Proc. Natl. Acad. Sci. USA
Vol. 92, pp. 1960–1964, March 1995
Biophysics

The thermoelastic basis of short pulsed laser ablation of biological tissue

(photomechanical ablation/nanosecond interferometry/spallation)

IRVING ITZKAN*, DOUGLAS ALBAGLI†, MARTA L. DARK, LEV T. PERELMAN, CHARLES VON ROSENBERG, AND MICHAEL S. FELD

Laser Biomedical Research Center, George R. Harrison Spectroscopy Laboratory, Massachusetts Institute of Technology, Cambridge, MA 02139

Communicated by Arthur Kantrowitz, Dartmouth College, Hanover, NH, November 2, 1994

ABSTRACT **Strong evidence that short-pulse laser ablation of biological tissues is a photomechanical process is presented. A full three-dimensional, time-dependent solution to the thermoelastic wave equation is compared to the results of experiments using an interferometric surface monitor to measure thermoelastic expansion. Agreement is excellent for calibrations performed on glass and on acrylic at low laser fluences. For cortical bone, the measurements agree well with the theoretical predictions once optical scattering is included. The theory predicts the presence of the tensile stresses necessary to rupture the tissue during photomechanical ablation. The technique is also used to monitor the ablation event both before and after material is ejected.**

Theory

Experimental results reported in the literature reveal that the energy density required to initiate ablation of biological tissue with nanosecond laser pulses is 10-fold less than that required for vaporization. This holds for a wide range of laser wavelengths (1, 2). When the laser pulse duration is shorter than a characteristic time, the material is "inertially confined"—i.e., it does not have time to expand, and heating takes place at constant volume.

For ablation using short-pulsed lasers, there is evidence that photomechanical effects play the most significant role (1, 3). Here it is presumed that, since most materials are weaker in tension than in compression, the material will fail wherever the induced tensile stresses exceed the tensile strength. A one-dimensional photomechanical model of laser-induced spallation correctly predicts the reduced energy density observed for nanosecond pulses. However, it also predicts that damage should first occur approximately one absorption depth beneath the surface (4, 5). In fact, ablation occurs at or near the surface. For the lasers and wavelengths used in ablating biological tissue, the optical absorption depth is usually comparable to the transverse laser dimension, and a one-dimensional approximation is not appropriate. One-dimensional estimates made by our group did not correctly predict the observed surface movement, although they did account for the order of magnitude decrease in the energy required to reach threshold (1, 6). The various discrepancies can be reconciled by including three-dimensional effects. We have solved the full time-dependent three-dimensional equations, which predict that significant tensile stresses are created on the surface, precisely where ablation is observed to occur. All the time scales considered are much shorter than the time associated with thermal relaxation.

When a material absorbs and is heated by laser energy, the resulting nonuniform temperature distribution causes internal forces, which lead to thermoelastic deformation. This deformation in a solid body is determined by the thermoelastic wave equation (7):

$$\rho\frac{\partial^2\mathbf{u}}{\partial t^2} - \frac{E}{2(1+\sigma)}\nabla^2\mathbf{u} - \frac{E}{2(1+\sigma)(1-2\sigma)}\nabla(\nabla\cdot\mathbf{u}) = \frac{-E\beta}{3(1-2\sigma)}\nabla T, \quad [1]$$

subject to the appropriate boundary and initial conditions, where $\mathbf{u}$ is the displacement vector, ρ is the density, E is Young's modulus, σ is Poisson's ratio, β is the thermal expansion coefficient, and T is the laser-induced temperature increase above a uniform ambient level. Eq. **1** is Newton's law with the mass (density) times the acceleration set equal to the elastic forces and the force generated by the thermal gradient. The laser-induced stresses can be determined from the displacement vector using the stress–strain relation, expressed here in standard tensor notation (7):

$$\sigma_{ik} = \frac{E}{1+\sigma}\left(u_{ik} + \frac{\sigma}{1-2\sigma}u_{jj}\delta_{ik}\right) - \frac{E\beta T}{3(1-2\sigma)}\delta_{ik}, \quad [2]$$

where σ_{ik} are the stresses, u_{ik} are the strains, and δ_{ik} is the Kronecker delta function.

We consider a cylindrical geometry with axial symmetry and a laser-induced temperature distribution with an exponentially decaying axial profile and Gaussian, "top-hat", or "rounded top-hat" radial profile. Fig. 1 shows the coordinate system used and the geometries of the initial temperature distributions at $t = 0$. Eqs. **1** and **2**, together with the boundary conditions σ_{zz} and $\sigma_{rz} = 0$ at $z = 0$, completely determine the problem. We define the aspect ratio, R, as the ratio of the laser beam radius, w, to the optical penetration depth, D. For $R \gg 1$ the problem approaches the one-dimensional case. As R approaches unity, as in the case of most laser-irradiated biological tissue, where both w and D are of the order of several hundred micrometers, three-dimensional considerations become essential.

We wish to know the laser-induced stresses in the material as a function of time and space. For subthreshold irradiation fluences, this problem can be divided into four time regimes, governed by (*i*) inertial confinement, (*ii*) a transient regime, (*iii*) a quasi-steady-state equilibrium, and (*iv*) relaxation via thermal conduction. In the first regime, the absorption of the short laser pulse is essentially a delta function in time. Since nothing has had time to move, the initial stresses can be found from Eq. **2** by setting all displacements and their first derivatives equal to zero. These stresses serve as the initial conditions for the second regime. In the second, or transient, regime, the material reconfigures itself to return the net force

The publication costs of this article were defrayed in part by page charge payment. This article must therefore be hereby marked "*advertisement*" in accordance with 18 U.S.C. §1734 solely to indicate this fact.

*To whom reprint requests should be addressed.
†Present address: General Electric Research and Development Center, Schenectady, NY 12301.

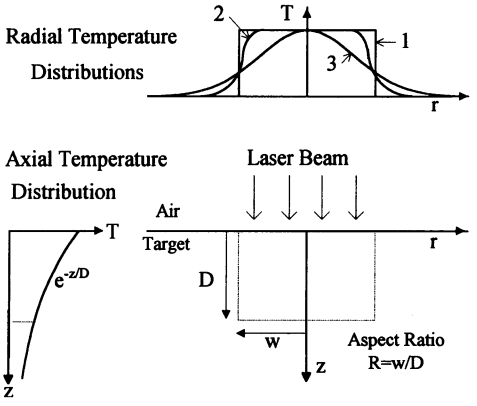

FIG. 1. A laser beam incident on a target surface creates a nonuniform temperature distribution within the target, which is a function of both the spatial distribution of the beam and the optical properties of the material. The resulting deformation and the associated stresses can be determined by solving the thermoelastic equations. The laser profiles shown are 1, top hat; 2, rounded top hat; i.e., a top hat with cosine function at the edges; 3, Gaussian. The defining equations for profile 2 are as follows: $T(r, z) = T_0 e^{-z/D}$, for $r \le r_1$; $T(r, z) = 0.5\ T_0 e^{-z/D}\{1 + \cos[\pi(r - r_3)/k_1]\}$, for $r_1 < r \le r_2$; and $T(r, z) = 0$, for $r > r_2$. In the equations, r_1, r_2, r_3, and k_1 are chosen to round the edge and keep the total energy the same as a top hat of radius w. For $w = 500\ \mu m$, the chosen values are $r_1 = 450\ \mu m$, $r_2 = 530\ \mu m$, $r_3 = 460\ \mu m$, and $k_1 = 77\ \mu m$.

to zero. This lasts for a period of time approximately equal to L/C, where C is the speed of sound in the material and L is a characteristic dimension of the problem. In this regime we use a fully time-dependent numerical solution obtained by integrating Eq. **1** on a spatially uniform grid using the Adams–Bashforth time stepping method (8, 9).

In the third, or quasi-steady-state, regime, the system reaches equilibrium, and the net force in any direction is zero. However, the individual stress components are not zero and can be appreciable. Even though the transients have ceased, quasi-steady-state thermoelastic stresses exist due to the persistence of the nonuniform temperature distribution. In this regime we have been able to obtain an analytical solution by setting $\partial^2\mathbf{u}/\partial t^2 = 0$ in Eq. **1** (10). We use this result to check that the numerical solution in regime 2 approaches the analytical solution in regime 3 as time approaches infinity. In the fourth, or thermal relaxation, regime, stresses decay to zero as thermal conduction causes the temperature distribution to become uniform. The thermal diffusivity of biological tissue is about the same as water, $\approx 0.0015\ cm^2/s$, which gives a thermal relaxation time of several hundred milliseconds for the dimensions considered here. Thus, thermal relaxation has no effect on the calculations in the first three regimes.

Calculations using the numerical solution provided two very significant pieces of information. The theoretically predicted movement normal to the surface, at the point ($z = 0, r = 0$), is a unique measure of the important optical and mechanical properties of the material. In Fig. 2 this numerically predicted surface expansion is shown as a function of time for a rounded top-hat laser profile and some typical material parameters. The rounded top-hat profile is used to avoid the problems associated with modeling sharp edges on a numerical grid. The location of the first peak, marked F_1, corresponds to the time for a longitudinal acoustic wave to reach the center from the beam edge and is therefore only a function of w and C_l, the longitudinal speed of sound. Since w is known, C_l can be determined. The location of the second peak, marked F_2, is related to the transverse speed of sound, C_t. Since $(C_t/C_l)^2 = (1 - 2\sigma)/(2(1 - \sigma))$, use of this relation and the known value of C_l allows the Poisson ratio to be determined from the second peak. Since the initial slope of the expansion curve,

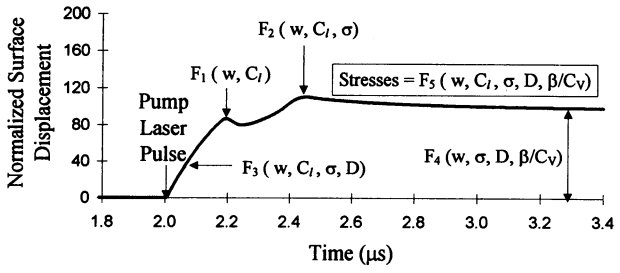

FIG. 2. The time evolution of the thermoelastic expansion at $z = 0$ and $r = 0$, predicted by the three-dimensional model, allows the determination of mechanical, optical, and thermal properties from features in the surface movement. These features also allow determination of the magnitude of the induced stresses. The calculation is performed for a typical material, and displacement is normalized so that the quasi-steady-state value is 100. Material properties: $C_l = 3000$ m/s, $\sigma = 0.25$, $D = 400$ mm, and $R = 1.25$.

marked F_3, is a function of w, C_l, σ, and D, the optical penetration depth, D, can now be determined. Using the quasi-steady-state equilibrium displacement, marked F_4, the ratio of the expansion coefficient to the heat capacity, β/C_v, can then be calculated. This calculation also yields the Grüneisen coefficient, $\Gamma = \beta C_l^2/C_v$, a parameter that appears in the equation of state for solids. Finally, all the stresses can be calculated from the now known parameters and displacements. Thus if we measure the time-dependent displacement at $z = 0$ and $r = 0$ at subthreshold fluences, we can determine all the physical parameters and stresses of the material under study.

The second significant result is that substantial tensile stresses are generated directly on the surface ($z = 0$), where ablation is observed to occur. Fig. 3 shows the time evolution of the radial stress on the surface as a function of radial position during the transient regime for the material parameters listed. The stress oscillates between compression and tension, and the tensile stresses are nearly 50% of the initial peak compressive stress. Also, good agreement between the quasi-steady-state analytical solution and the numerical solution at 2500 ns is illustrated.

The analytical solution reveals that important tensile stresses also persist into the quasi-steady-state regime. Fig. 4 shows that the quasi-steady-state circumferential stress contains a large tensile component on the surface just outside the irradiated area for a top-hat initial temperature distribution. The confined hot material is attempting to force the cold surrounding material outward. Even though the quasi-steady-state stresses are smaller than the transient stresses, they

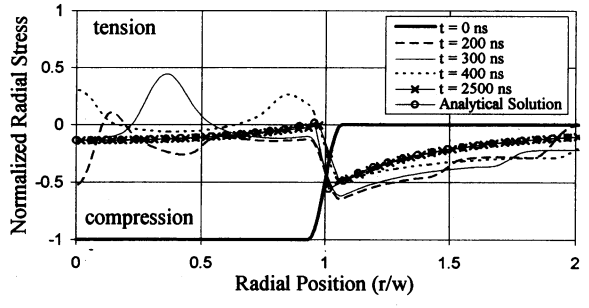

FIG. 3. The time evolution of radial stress on the surface ($z = 0$) as a function of radial position during the transient time regime. Geometric constants: $R = 0.70$, $D = 860\ \mu m$, $w = 600\ \mu m$. Material constants: $\rho = 1.2\ g/cm^3$, $C_l = 2850$ m/s, $\sigma = 0.25$. Tensile stresses are positive, and compressive stresses are negative. All stresses are normalized to $|\sigma_{max}|$, the initial compressive stress at the surface, where $\sigma_{max} = -E\beta T(r = 0, z = 0)/3(1 - 2\sigma)$. Note that the peak tensile stresses reach values nearly 50% of $|\sigma_{max}|$. At 2000 ns the stresses are at their quasi-steady-state values.

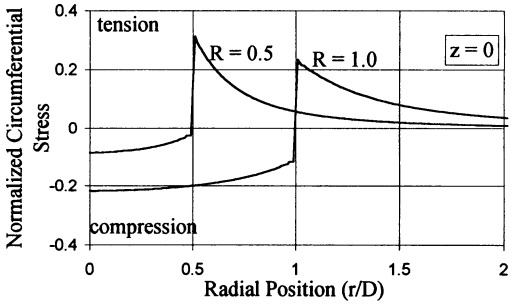

FIG. 4. The surface circumferential stress for a top-hat temperature distribution as a function of radial position is given for two aspect ratios, $R = 0.5$ and 1, during the quasi-steady-state period. Material constants: $\rho = 1.2$ g/cm^3, $C_l = 2850$ m/s, $\sigma = 0.25$. As in Fig. 3, all stresses are normalized to $|\sigma_{max}|$, and tensile stresses are positive. The substantial tensile "hoop" stresses located just outside the beam boundary can cause significant damage, even in the nonirradiated region, especially since they persist for very long times.

persist for eight orders of magnitude longer in time. Experimental evidence shows that both the amplitude of the stress and the time over which the stress operates are important. A general dynamic fracture criterion has been introduced by Tuler and Butcher, given a time-dependent tensile stress, $\sigma_{ii}(t)$ (11):

$$\int[\sigma_{ii}(t) - \sigma_i]^\lambda dt = K, \qquad [3]$$

where λ and K are constants and σ_i is a stress threshold below which fracture would not occur, even for long times. This formula states that fracture occurs when the cumulative product of stress above threshold to the λ power and time reaches some critical value, K (λ was empirically determined to be ≥ 1). The dynamic fracture criterion suggests that smaller amplitude, long-lived stresses may play an important role in the damage observed in the so called "heat-affected zone", which is often seen in the region surrounding the ablation center.

The foregoing considerations show that an experiment that can measure surface displacement with sufficient time and spatial resolution would be of significant value. First, by using materials whose physical parameters are well known, we can establish that the theory is correct, that the experiment is working properly, and that the material is behaving thermoelastically from low fluences up to ablation threshold. Glass and cortical bone proved to be such materials. Second, by observing deviations from the expected behavior, new effects can be observed. Acrylic proved to have a nonlinear behavior with increasing fluence. Human meniscus proved to have a major deviation from the expected behavior; it showed the onset of an additional phenomenon, cavitation. The results obtained for meniscus and for water doped with an absorbing dye are discussed in ref. 12. Third, the results yield a quantitative measure of the physical parameters of biological materials, which can be difficult to obtain by other techniques. The experiment described below was developed to achieve these objectives.

Experiment

The apparatus consisted of an interferometric surface-monitoring probe and an intense pump laser to provide the thermal input pulse. A detailed schematic of the latest model can be found in ref. 12. An earlier version is described in ref. 13. This technique can measure the laser-induced surface movement of a target material with a spatial resolution of ≈ 3 nm and a temporal resolution of ≈ 3 ns. The pump laser-induced thermoelastic expansion is measured by a Michelson interferometer, which uses a He-Ne probe laser; the sample is the end mirror in one arm, and a rotating corner cube prism is included in the reference arm. By causing the reference arm length to vary at a constant velocity, the system is given a built-in bias, which allows the direction as well as the speed to be measured; thus, the surface position as a function of time can be determined. The pump is a 7.5-ns, frequency tripled, Q-switched Nd:YAG laser operating at a wavelength of 355 nm, which is passed through a beam homogenizer to create a uniform spatial profile. The most uniform portion of the beam is selected with a 3-mm aperture, which is then demagnified and reimaged onto a spot on the target surface whose diameter can be varied from 750 μm to 1 mm. The pump laser energy is controlled via a half-wave plate and a Glan polarizing prism. The 100-μm diameter probe beam can be positioned anywhere along the pump beam radius to sample the motion as a function of radial position.

Experimental data were collected for several materials, including an acrylic (acrylite FF; Cyro, Mt. Arlington, NJ) and a glass filter (GG 375; Schott, Duryea, PA). For the acrylic sample used, we measured an optical penetration depth of $D = 1000$ μm, and for the glass filter $D = 480$ μm. Bovine tibial cortical bone was scraped of excess soft tissue and the periosteum, polished to obtain a smooth surface for better light reflection, and refrigerated at 4°C until use. Experiments were performed at room temperature.

Results

Fig. 5 shows results for the surface movement of acrylic as a function of time for several different subthreshold fluences. The surface displacement increases with fluence, but the temporal features remain constant, as shown in the figure, where the motion is normalized to a quasi-steady-state value of 100 for all fluences. As shown, all the features previously described agree very well with the theory. The measured quasi-steady-state values are plotted in Fig. 6 versus fluence for acrylic and glass. The expected relation between fluence and displacement is linear. Also in this figure is the theoretically predicted value of this linear relationship as calculated from the manufacturer's data for these materials, with no free parameters. For glass, the agreement is excellent, even to ablation threshold. In acrylic, there is initial agreement at low fluences, but an as yet undetermined nonlinear effect causes the displacements to be lower than expected at high fluences. Also, for acrylic there is a larger spread in the data with each subsequent shot at the same location, each one producing less thermoelastic expansion. Small permanent defects, which can be seen with a microscope, are created in acrylic by subthreshold laser pulses. No such defects are observed in glass.

The acrylic samples were studied microscopically, and a large number of defects were observed (9). The defects under high magnification appear to be fracture patterns. The defects are concentrated near the surface of the sample, and the

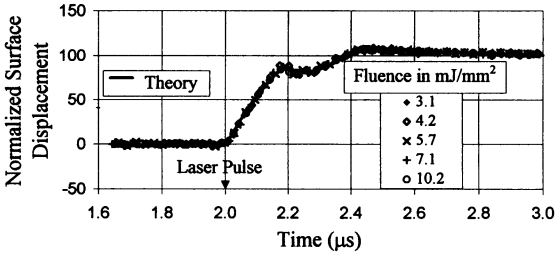

FIG. 5. The measured surface movement at $r = 0$ of acrylic after subthreshold laser irradiation compared to theoretical predictions, for five fluences with the quasi-steady-state value normalized to 100. Material properties: $C_l = 2550$ m/s, $\sigma = 0.32$, and $D = 1$ mm. Pump laser radius is $w = 500$ μm.

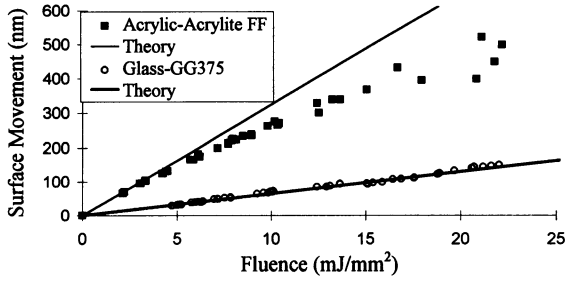

FIG. 6. Quasi-steady-state displacements of acrylic and glass as a function of fluence. For acrylic, $R = 0.5$ and $D = 1.0$ mm. Manufacturer's data: $\rho = 1.2$ g/cm^3, $C_v = 1.47$ J/g·K, $\beta = 192 \times 10^{-6}$/K, $\sigma = 0.32$. For glass, $R = 1.04$ and $D = 480$ μm. Manufacturer's data: $\rho = 2.61$ g/cm^3, $C_v = 0.72$ J/g·K, $\beta = 27.0 \times 10^{-6}$/K, $\sigma = 0.235$.

number of defects increases with subsequent laser pulses. Defect formation also correlates with the nonlinear fall-off of equilibrium displacement as a function of fluence shown in Fig. 6. Since these fractures weaken the overall strength of the acrylic, their accumulation may play a significant role in the ablation process, which has been called the "incubation effect," where a material does not seem to be affected by n pulses at a given subthreshold fluence but then ablates on the $n + 1$ pulse.

We studied the onset of ablation in cortical bone, a tissue whose behavior is similar to that of acrylic. Fig. 7 shows typical surface displacement of bone. The equilibrium displacement was normalized to 100 for each fluence, and again the time-dependent behavior is identical throughout the range of fluences. The theoretically predicted movement, based on the values of C_l, σ, and D determined as in Fig. 2, is compared to the measured movement in Fig. 7. Although there is general agreement between the two curves, the predicted alternating contractions and expansion are "washed out." For a turbid medium such as bone, scattering within the target will change the temperature distribution and blur the sharp temperature gradient at the radial edge of the laser beam. From ref. 14, the value $\mu_a = 0.7$ mm^{-1} for the absorption coefficient was obtained, and using the determined value of D, the effective scattering coefficient was inferred to be $\mu_s' = 3.7$ mm^{-1}. The anisotropy parameter, g, was chosen to be 0.8, a typical value for biological tissue, and the temperature distribution was calculated numerically using these values in a Monte Carlo calculation (15). As expected, scattering of the light from within the laser beam boundary leads to a reduction of temperature in the center and an increased temperature at larger radii. The predicted thermoelastic surface motion of the bone, using the new temperature distribution, is also plotted in Fig. 7. The agreement between theory and experiment is

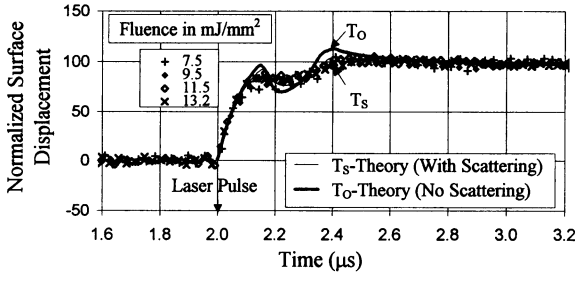

FIG. 7. Surface movement of cortical bone compared to theoretical predictions ($w = 500$ μm, $C_l = 3000$ m/s, $\sigma = 0.35$, $D = 325$ μm). Two theoretical curves are shown: the arrow marked T_o denotes the original theoretical curve and the arrow labeled T_s points to the theoretical curve which includes a correction due to optical scattering. Four different fluences are displayed with quasi-steady-state values normalized to 100.

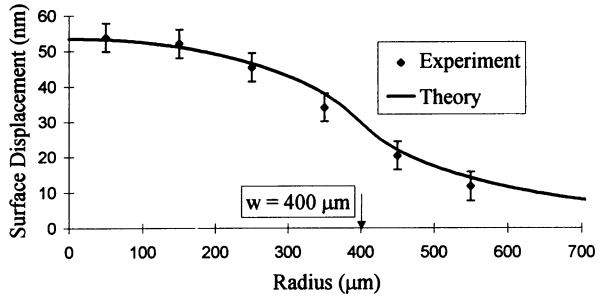

FIG. 8. By repositioning the probe beam along a radius of the irradiated spot, the displacement of bone as a function of radial position can be measured. The quasi-steady-state values are plotted, along with the theoretical value obtained, by including scattering effects in the calculation as in Fig. 7. The beam radius is $w = 400$ μm.

considerably improved when scattering effects are taken into account, which lends credence to the hypothesis that scattering is responsible for the washing out of the small expansions and contractions.

In the apparatus, the probe beam can be translated across the sample's surface relative to the pump beam, so that it can be positioned at different radii. Fig. 8 shows the radial profile of surface expansion of bone. The radius of the pump beam is 400 μm, and surface displacement is measured from the center to 550 μm. Even though the material receives no laser irradiation at this distance from center, it shows displacement because it is pulled up by the "hot" adjacent material. Off-center monitoring also allows us to observe the behavior of the rim during ablation. Although the surface is destroyed once ablation occurs and material is ejected, we can monitor the surface outside the irradiated area ($r > w$) to determine when ablation occurs. Fig. 9 shows the motion of bone just outside the irradiated area when irradiated with sufficient energy to cause ablation, compared to the subthreshold theoretical curve. Ablation occurs at a time about 350 ns after the laser pulse. There is an abrupt departure from the theoretical curve; the surface at the rim undergoes a large contraction to a position 200 nm below the original surface position, followed by a slow recoil expansion for several microseconds to the limit to which we monitored time in this measurement. This experiment was repeated for acrylic, and surface damage was observed under a microscope. The appearance of surface damage always corresponded with the large negative surface motion of the rim.

Conclusions

Interferometric surface monitoring is a significant tool for studying the fundamental mechanisms of ablation of biological

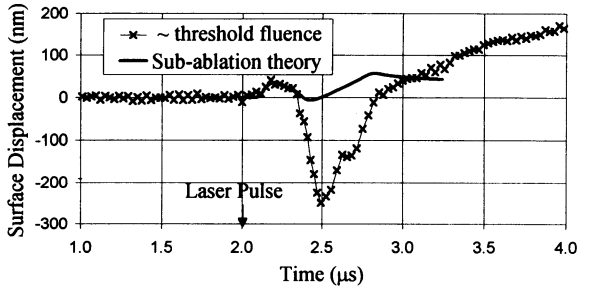

FIG. 9. Ablation of bone is monitored by placing the He-Ne probe beam outside of the laser-irradiated area ($w = 400$ μm, $r = 700$ μm). The fluence used, 35.4 mJ/mm^2, is the threshold value for causing ablation. At about 350 ns after the laser pulse, the cold rim recoils to a depth of -250 nm and then expands. These motions are very large compared to the subthreshold values and appear only when ablation occurs.

tissue. A three-dimensional theoretical model for thermoelastic surface expansion after subablation threshold laser irradiation has been developed, which establishes the relationship of this movement to important mechanical and optical properties of the tissue. The surface movement of bone, glass, and acrylic were measured after irradiation with a 7.5-ns, 355-nm pulse. The results for glass and acrylic were quantitatively consistent with the theoretical model presented, although acrylic did show a deviation from theory as defects were formed in the material. The results for bone were in good agreement with the theory after the effects of scattering in a turbid medium were taken into account. Finally, the interferometric surface monitoring technique has the ability to monitor the ablation event by placing the probe beam outside of the pump beam area. This technique will be useful in studying many aspects relating to tissue ablation. In particular, it could be used to measure the important physical properties of biological tissue, knowledge of which is necessary to understand how biological tissue responds to laser ablation.

We thank our colleagues of the Lester Wolfe Angiosurgery Group at Massachusetts Institute of Technology. This work was supported by the National Institutes of Health (Grant RR02594) through the administration of the Massachusetts Institute of Technology Laser Biomedical Research Center.

1. Albagli, D., Perelman, L. T., Janes, G. S., von Rosenberg, C., Itzkan, I. & Feld, M. S. (1994) *Laser Life Sci.* **6,** 55–68.
2. Oraevsky, A. A., Esenaliev, R. I. & Letokhov, V. S. (1991) in *Laser Ablation, Mechanisms and Applications*, eds. Miller, J. C. & Haglund, R. F., Jr. (Springer, New York), Vol. 389, pp. 112–122.
3. Itzkan, I., Albagli, D., Banish, B. J., Dark, M., von Rosenberg, C., Perelman, L. T., Janes, G. S. & Feld, M. S. (1994) *AIP Conf. Proc.* **288,** 491–506.
4. Dingus, R. S. & Scammon, R. J. (1991) in *Laser Ablation, Mechanisms and Applications*, eds. Miller, J. C. & Haglund, R. F., Jr. (Springer, New York), Vol. 389, pp. 180–190.
5. Dingus, R. S. & Scammon, R. J. (1991) *J. Soc. Photo–Opt. Instrum. Eng.* **1427,** 45–54.
6. Albagli, D., Banish, B., Dark, M., Janes, G. S., von Rosenberg, C., Perelman, L. T., Itzkan, I. & Feld, M. S. (1994) *Laser Surg. Med.* **14,** 374–385.
7. Landau, L. D. & Lifshitz, E. M. (1986) *Theory of Elasticity* (Pergamon, Oxford), pp. 13–92.
8. Potter, D. (1977) *Computational Physics* (Wiley, New York), pp. 40–79.
9. Albagli, D. (1994) Ph.D. thesis (Massachusetts Institute of Technology, Cambridge).
10. Albagli, D., Dark, M., von Rosenberg, C., Perelman, L. T., Itzkan, I. & Feld, M. S. (1994) *Med. Phys.* **21,** 1323–1331.
11. Tuler, F. R. & Butcher, B. M. (1968) *Int. J. Fract. Mech.* **4,** 431–437.
12. Schaffer, J. L., Dark, M., Itzkan, I., Albagli, D., Perelman, L. T., von Rosenberg, C. & Feld, M. S. (1994) *Clin. Orthop.*, in press.
13. Perelman, L. T., Albagli, D., Dark, M., Schaffer, J. L., von Rosenberg, C., Itzkan, I. & Feld, M. S. (1994) *J. Soc. Photo–Opt. Instrum. Eng.* **2134,** 144–155.
14. Izatt, J. A. (1991) Ph.D. thesis (Massachusetts Institute of Technology, Cambridge).
15. Wu, J., Partovi, F., Feld, M. S. & Rava, R. P. (1993) *Appl. Opt.* **32,** 1115–1121.